3D crustal structure of the Ligurian Sea revealed by ambient noise tomography using ocean bottom seismometer data

Felix Noah Wolf[1], Dietrich Lange[1], Anke Dannowski[1], Martin Thorwart[2], Wayne Crawford[3], Lars Wiesenberg[2], Ingo Grevemeyer[1], Heidrun Kopp[1,2], and the AlpArray Working Group[+]

5

[1] GEOMAR Helmholtz Centre for Ocean Research Kiel, Kiel, 24148, Germany
[2] Institute of Geosciences, Kiel University, Kiel, 24118, Germany
[3] Laboratoire de Géosciences Marines, Institut de Physique du Globe de Paris, Paris, 75238 Cedex 5, France
[+] A full list of team members appears at the end of the paper.

10 *Correspondence to*: Felix N. Wolf (fnwolf@geomar.de)

Abstract. The Liguro-Provençal basin was formed as a back-arc basin of the retreating Calabrian-Apennines subduction zone during the Oligocene and Miocene. The resulting rotation of the Corsica-Sardinia block is associated with rifting, shaping the Ligurian Sea. It is still debated whether oceanic or atypical oceanic crust was formed or if the crust is continental and experienced extreme thinning during the opening of the basin. We invert velocity models using an amphibious network of
15 seismic stations, including 22 broadband Ocean Bottom Seismometers (OBS) to investigate the lithospheric structure of the Ligurian sea. The instruments were installed in the Ligurian Sea for eight months between June 2017 and February 2018 as part of the AlpArray seismic network. Because of additional noise sources in the ocean, OBS data are rarely used for ambient noise studies. However, we attentively pre-process the data, including corrections for instrument tilt and seafloor compliance. We took extra care to exclude higher modes of the ambient-noise Rayleigh waves. We calculate daily cross-correlation
20 functions for the LOBSTER array and surrounding land stations. Additionally, we correlate short time windows that include teleseismic earthquakes that allow us to derive surface wave group velocities for longer periods than using ambient noise only. Group velocity maps are obtained by inverting Green's functions derived from the cross-correlation of ambient noise and teleseismic events, respectively. We then used the resulting 3D group velocity information to calculate 1D depth inversions for S-wave velocities. The shear-wave velocity results show a deepening of the Moho from 12 km at the southwestern basin
25 centre to 20-25 km at the Ligurian coast in the northeast and over 30 km at the Provençal coast. We find no hint on mantle serpentinisation and no evidence for an Alpine slab, at least down to depths of 25 km. However, we see a separation of the southwestern and northeastern Ligurian Basin that coincides with the promoted prolongation of the Alpine front.

1 Introduction

30 The Ligurian Sea is a marginal basin located in the north-western Mediterranean Sea at the transition from the Alpine orogen to the Apennine system (Fig. 1). It formed as a back-arc basin to the south-eastward trench retreat of the Apennines-Calabrian subduction zone during the late Oligocene and Miocene (Gueguen et al., 1998; Rollet et al., 2002). Rifting in the Liguro-

Provençal basin initiated about 32 Ma ago (Jolivet et al., 2015). From 21 Ma on, the rifting was followed by a counter-clockwise rotation of the Corsica-Sardinia block (Jolivet and Faccenna, 2000; Rollet et al., 2002) by approximately 30 degrees
35 (Vigliotti and Langenheim, 1995). Gattacceca et al. (2007) estimate a rotation of 45 degrees, based on ^{40}Ar/^{39}Ar geochronological investigations of Miocene volcanic sequences in Sardinia. At the end of the Burdigalian Age (about 16-18 Ma), the Corsica-Sardinia block collided with the Apennines (Rosenbaum et al., 2002). The opening of the Ligurian Sea terminated, while the roll-back of the Calabrian subduction zone continued and initiated the opening of the Tyrrhenian Sea (e.g. Faccenna et al., 2001). Today, the Ligurian Sea is 150-225 km wide, while the basin itself has a width of 70-170 km
40 (Dannowski et al., 2020). The continental margin is narrow and steep at the Ligurian coast but broader on the Corsican side. Whether continental crust was extremely thinned during the rifting or oceanic spreading occurred and formed oceanic crust in the basin centre was addressed in many studies. Several authors (Rollet et al., 2002; Gailler et al., 2009; Jolivet et al., 2015) propose an area of atypical oceanic crust, characterised as being very thin (< 4 km) and showing complex magnetic anomalies that can not be correlated to isochrons (Rollet et al., 2002), in the basin-centre. This area is neighboured by a broad transition
45 zone towards continental crust at the basin's edges. Based on a recent refraction seismic study, Dannowski et al. (2020) propose that seafloor spreading was not initiated during the formation of the Ligurian Basin. They show that towards the southwest of the basin the continental crust thins and possibly gives way to partly serpentinised mantle lying directly beneath an up to 7 km thick sediment cover. Schettino & Turco (2006) find a similar sediment thickness based on a joint interpretation of magnetic and seismic data.

50 Another open question is related to the location of the prolongation of the Alpine front. It is well defined onshore Italy and Corsica, but it remains unclear if and where the connection of these parts of the front is preserved offshore. At the scale of the entire Alpine belt region, land data based ambient noise tomographies have been performed by Molinari et al. (2015b), Kästle et al. (2018) and Lu et al. (2018). These studies revealed the onshore geometry but did not cover the Ligurian Sea. Guerin et al. (2020) conducted an ambient noise surface-wave tomography along the southwestern Alps and a small part of the Ligurian
55 margin using five ocean bottom seismometers (OBS) and two offshore cabled seismometers close to Nice. They identify a low-velocity zone offshore Nice that is linked to salt and evaporite deposits.

To better understand the evolution of the Ligurian Basin and the processes driving its formation and controlling its deep-seated roots, we use a unique amphibious seismic network covering the entire Ligurian Sea and adjacent coastal areas, providing high-resolution group velocity maps and a three-dimensional shear velocity model.

Solid Earth
Discussions
Open Access
EGU
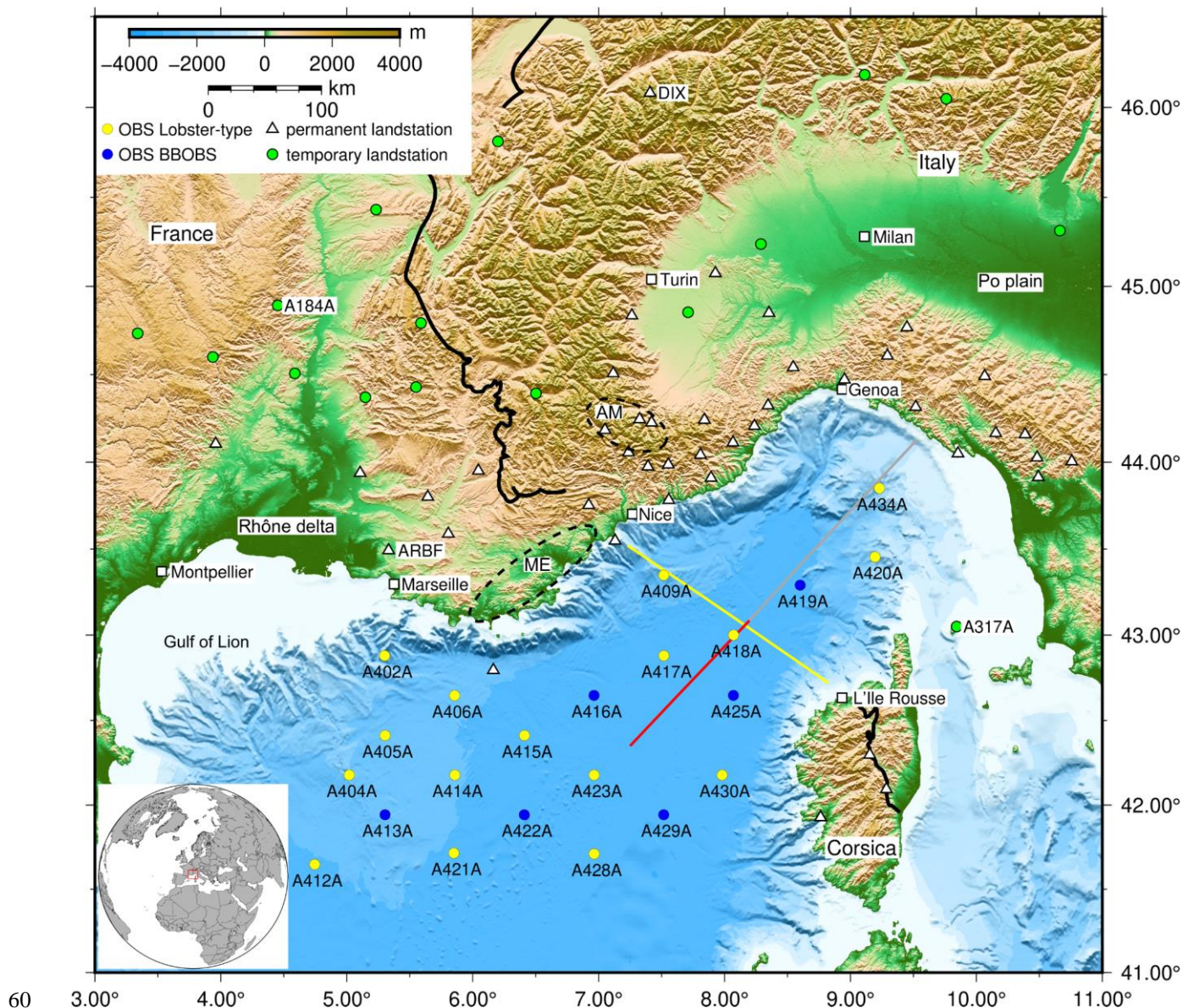
Figure 1: Map of the Ligurian Sea and adjacent Alpine region and the stations used for this study. OBS stations (network code: Z3) are shown as yellow (Lobster-type) and blue (BBOBS) circles. Permanent land stations (network codes: CH, FR, GU, IV, and MN) are shown as white triangles. Temporary land stations from AlpArray (network code: Z3) are shown as green circles. White squares represent cities. The black line represents the Alpine front (Schmid et al., 2004), AM marks the Argentera Massif, and ME marks the Maures-Esterel Massif. The inlay map in the bottom left shows the location of the research area (red box). The red, grey, and yellow lines show seismic refraction and reflection lines; red: Dannowski et al. (2020), grey: Makris et al. (1999), yellow: LISA01, Contrucci et al. (2001). The topography is plotted based on a GRMT grid (Ryan et al., 2009).

Solid Earth
Discussions
Open Access
EGU

70

2 Data

A network of 29 broadband ocean-bottom seismometers (OBS) was installed jointly by IPGP (Paris, France), ISTerre (Grenoble, France) and GEOMAR (Kiel, Germany) (Fig. 1) to investigate the velocity structure of the crust and upper mantle beneath the Ligurian Sea. The LOBSTER (**L**igurian **O**cean **B**ottom **S**eismology & **Te**ctonic **R**esearch) array is the offshore

75 component of the AlpArray seismic network (Hetényi et al., 2018). The instruments were deployed from the RV *Pourquoi Pas?* in June 2017 and were recovered in February 2018 by RV *Maria S. Merian*. 28 stations were recovered. Twenty-two stations provided a complete dataset. The LOBSTER network consisted of seven French OBS (BBOBS), 12 OBS (Lobster-Type) provided by the German instrument pool (DEPAS) and 10 OBS (Lobster-Type) from GEOMAR, Germany. The BBOBS were equipped with three-component broadband Nanometrics Trillium 240 broadband seismometers with a lower corner

80 period of 240 s and a differential pressure gauge (DPG) designed by the Scripps Institution of Oceanography (Cox et al., 1984). The sampling rate of the installed LCHEAPO recorder was 62.5 Hz. The DEPAS OBS and five GEOMAR OBS were equipped with Trillium compact seismometers by Nanometrics Inc. with a lower corner period of 120 s and HTI-01-PCA hydrophones from High Tech Inc. The sampling rate of the K.U.M. 6D6 recorder was 250 Hz.

The instrument clocks were synchronised with GPS time before deployment and after recovery to reveal any internal clock

85 drift and apply a linear clock drift correction. We calculated probabilistic power spectral densities (PPSDs) for every station (McNamara and Buland, 2004). The lowest spectral levels on the vertical seismometer components fall in between the mean minimum and maximum noise levels for land stations (Peterson, 1993) for both the German (Fig. S1 a-b) and French OBS (Fig. S1 c-d). Regarding the pressure component, the French DPGs yield high-quality data (-38 dB to 40 dB) while the HTI hydrophones have a range of -20 dB to 40 dB with a lesser resolution for periods larger than 10 s (Fig. S1 a, c). These results

90 are comparable to similar instrument setups (Stähler et al., 2016) used during the RHUM-RUM OBS experiment in the Indian Ocean. To resolve the entire structure of the Ligurian Sea and the surrounding areas onshore, we incorporated parts of the AlpArray land network plus 16 temporary and 42 permanent land stations in our analysis (Table S1).

3 Methods

The ambient noise technique was developed during the last 20 years (Lobkis & Weaver, 2001; Wapenaar et al., 2010a;

95 Wapenaar et al., 2010b) and is based on the concept of Aki (1957) regarding the spectra of stationary stochastic waves. Ambient noise techniques exploit the 'noise' of long-term recordings as the desired signal. This part of the measured signal includes, for example, anthropogenic noise, microseismic signals from ocean-coast interactions, and highly-scattered waves of teleseismic origin (Campillo and Paul, 2003; Campillo and Roux, 2016). Given a continuous measurement and uniformly distributed noise sources, the cross-correlation of recordings of two stations is used as the empirical Green's function

100   representing the subsurface response to a wave propagating from one station to the other. These empirical Green's functions from different station pairs are used to invert for two-dimensional (2D) group velocity maps, 1D velocity-depth profiles or 3D velocity distribution maps.

Although the technique is well established for land data (e.g. Barmin et al., 2001; Campillo & Paul, 2003; Shapiro et al., 2005; Prieto et al., 2009; Goutorbe et al., 2015; Kästle et al., 2019), there is no established routine for ambient noise analysis on

105   ocean bottom seismometer data. Previous studies show that ambient noise can be calculated using OBS data (e.g. Harmon et al., 2007, 2012; Takeo et al., 2014; Dewangan et al., 2018). However, compared to land stations, seismic recordings on OBS contain less anthropogenic noise but other additional noise sources like tilt and compliance noise (Crawford et al., 1998; Webb, 1998; Bell et al., 2015).

3.1 Pre-processing - tilt and compliance correction

110   Adimah & Padhy (2020) showed that reducing tilt and compliance noise before running the cross-correlation proves beneficial, as tilt and compliance noise are not part of the useful signal. Therefore, we pre-process the OBS data as proposed by Crawford & Webb (2000). First, we cut the continuous OBS recordings into daily files and resample the data at 1 Hz. Next, we remove tilt and compliance noise. Tilt noise is introduced by a slight inclination of the instrument, causing horizontal signals to appear on the vertical component (Crawford & Webb, 2000). Although the instruments level themselves to an accuracy of ±0.5°

115   (Lobster-Type) and ±5° (BBOBS), respectively, the remaining tilt is sufficient to create tilt noise. The tilt of the instrument can be caused by processes such as ocean bottom currents. On the other hand, compliance is a signal generated by ocean infragravity waves introducing pressure fluctuations that cause µm-scale deformation of the seafloor (Webb and Crawford, 1999). The variations of the gravitational forces of the water column, the deformation of the seafloor itself, and the caused variation in the distance of the OBS to the earth's gravitational centre all introduce changes to the measured acceleration

120   (Crawford et al., 1998). Thus, compliance leads to an increased vertical acceleration noise level by 10 dB to 25 dB for 30-100 s (Webb and Crawford, 1999).

To correct for tilt and compliance noise, we applied the procedure described in Crawford & Webb (2000) and Bell et al. (2015). First, we calculate a transfer function between the vertical seismometer component and the hydrophone component. Next, we subtract the coherent part of the signal (in this case: compliance) from the vertical seismometer component. We also corrected

125   both horizontal components for compliance before removing tilt noise (Crawford & Webb, 2000). Subsequently, the same routine is used to remove the coherent signal between the vertical component and each horizontal component to remove tilt noise. Thus, we calculate the transfer functions between the vertical component and each of the horizontal components. Finally, we obtain a vertical component corrected for tilt and compliance. The order in which the components are corrected is interchangeable. The land station recordings were not corrected for tilt and compliance noise but are also resampled to 1 Hz.

130

3.2 Ambient noise technique – cross-correlation and mode identification

Cross-correlation

We use the tilt- and compliance-corrected daily files to estimate cross-correlation functions (CCF) for every vertical component OBS-OBS station pair (Bensen et al., 2007). These CCFs are complemented by CCFs for selected OBS-land station pairs and

135 land-land pairs to obtain cross-correlations in other ray directions than those of the OBS-land pairs (Fig. 2). Additionally, we calculate CCFS for all land-land pairs for the land stations A317A, ARBF, and DIX (see Fig. 1) and CCFs for all combinations of 20 selected land stations (namely AJAC, BLAF, BOB, BSTF, CALF, CARD, EILF, ENR, GBOS, IMI, ISO, MSSA, PCP, PLMA, ROTM, SAOF SMPL, TRBF, TURF, and VLC) to increase the resolution onshore. The cross-correlation is calculated day-wise for every station pair. Afterwards, we stack the single-day CCFs to estimate one CCF per station pair.

140 In addition to ambient noise cross-correlations, we correlate time windows (45 min long) that include strong teleseismic events using the two-station method (e.g. Meier et al., 2004, Tonegawa et al., 2020). We only use station pairs for which the stations' azimuth equals the great circle from the event to within ± 7 °. The correlation window, starting at the origin time of the event, is dominated by the earthquake signals. The further processing is identical to correlating ambient noise day files but is performed for longer periods (20 s to 90 s).
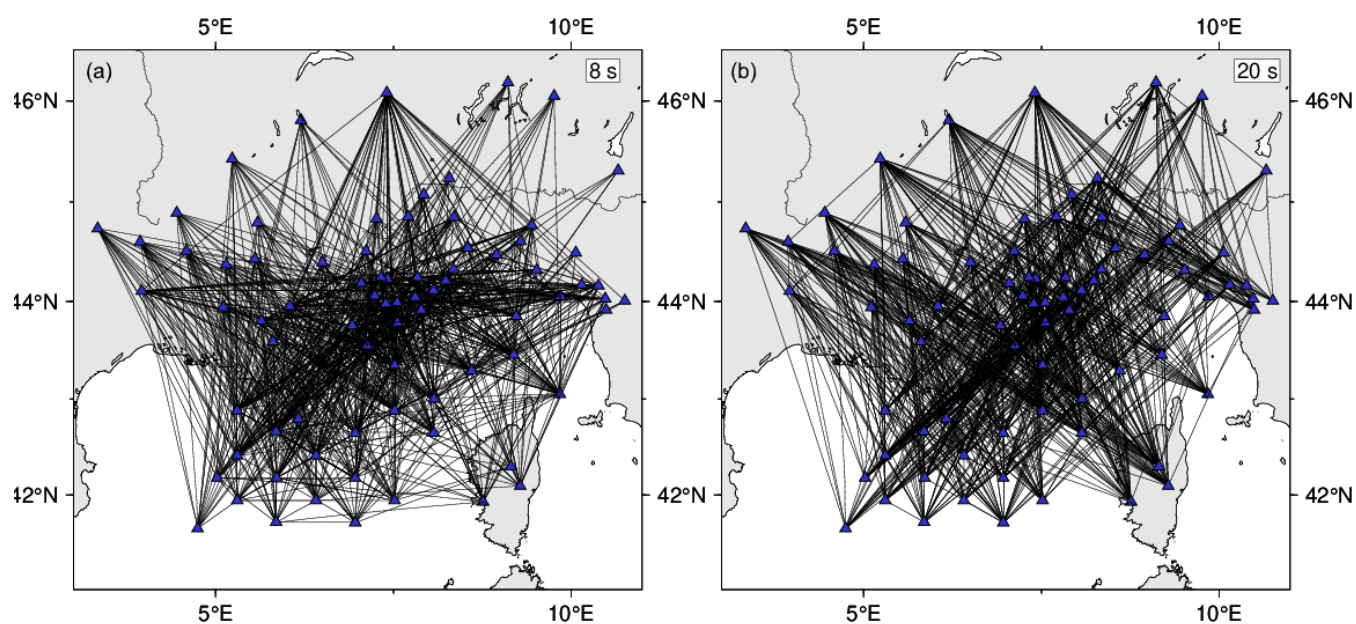
145

Figure 2: Ray coverage for ambient noise CCF-pairs at 8 s (a) and teleseismic CCF pairs at 20 s (b). Stations are marked as blue triangles.

150

Group velocity dispersion curves - fundamental mode and higher modes

To estimate group velocity dispersion curves, we apply the multiple filter technique (MFT) (Dziewonski et al., 1969). A narrow bandpass filter is applied to the CCFs to derive the velocity for a distinct period from the maximum correlation (e.g. Meier et al., 2004).

155   Extra care has to be taken when picking the dispersion curves since for some station pairs the first higher mode has stronger amplitudes than the fundamental mode. Different modes have different sensitivity kernels (e.g. Harmon et al., 2007), and, unfortunately, our tomography program cannot process input data from more than one mode at a time. Therefore, we picked manually by comparing each ray path to the theoretical dispersion curves predicted from the v_P-model from Dannowski et al. (2020) and PREM (Dziewonski and Anderson, 1981) (see white lines in Fig. 3).
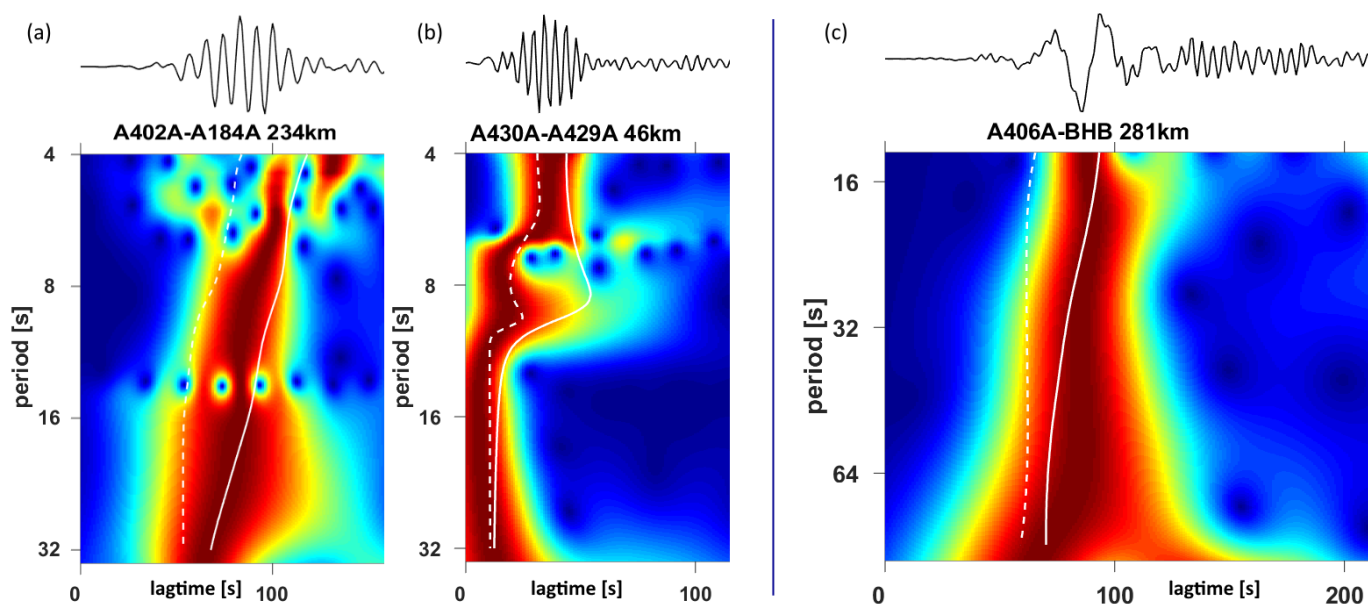
160

Figure 3: MFT examples for correlations on a) OBS-land pair, b) OBS-OBS station pair (both ambient noise cross-correlations), and c) land-land station pair (cross-correlation containing teleseismic event). The solid white line shows the theoretical fundamental mode; the dashed white line shows the theoretical first higher mode. In a) the fundamental mode fits the theoretical velocities, in b) the first higher mode correlates most strongly. Therefore, this pair was excluded from the tomography.

165   First, we picked the maximum signal on all dispersion curves. After comparing the group velocities with synthetic dispersion curves, we excluded about 100 station pairs that showed velocities likely related to higher modes (Fig. 3b). Higher modes were mainly observed for ray paths located in the southern part of the Ligurian Basin and parallel to the basin axis (Fig. 4). The origin could be layers in which the first higher mode couples more strongly than the fundamental mode, as previously observed by Takeo et al. (2014) for CCFs from OBS in the NW Pacific. During the MFT revision, we did not observe a degradation of

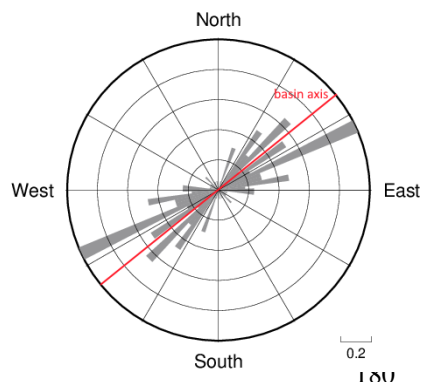170   the signal depending on the station distance.

7

Figure 4: Rose diagram of ray path azimuths showing the striking directions of the higher modes. The red line indicates the basin axis.

The identification and rejection of the higher mode dispersion curves resulted in 1342 dispersion curves for the fundamental mode from ambient noise CCFs and additional 1963 dispersion curves from teleseismic CCFs (Fig. 5) that were used for further analysis steps (Table S2). We use the ambient noise CCFs to derive dispersion curves for periods from 4-15 s. The CCFs from the correlation of teleseismic events were used to derive dispersion curves from 20-90 s (Fig. 5). The frequency bands of the dispersion curves are complementary and together provide a bandwidth ranging from 4-90 s.
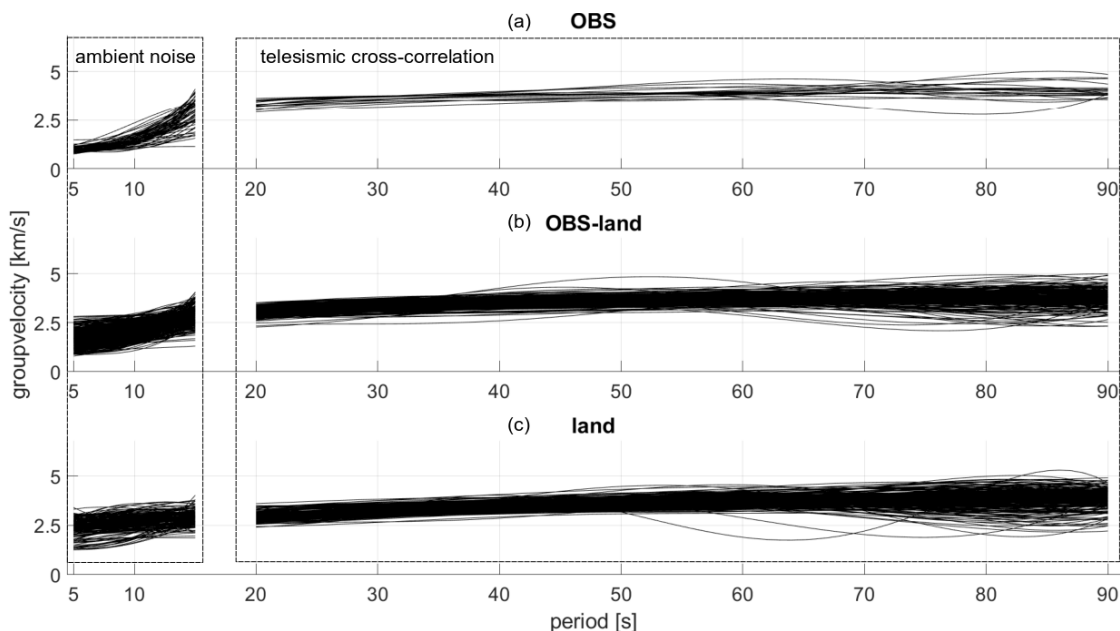
Figure 5: Picked dispersion curves from ambient noise cross-correlation and correlation of teleseismic events. The dispersion curves are sorted for different types of station pairs: (a) OBS-OBS pairs, (b) OBS-land pairs and vice versa, (c) land-land pairs.

Solid Earth
Discussions

3.3 Surface wave tomography for group velocities of ambient noise data and teleseismic data

195   We use the Fast Marching Surface Tomography method (FMST, Rawlinson & Sambridge, 2004, 2005) to derive 2D Rayleigh group velocity maps from the picked dispersion curves. FMST inverts for 2D map slices of group velocities for a given period. The forward prediction of travel times is achieved using the fast marching method (Sethian, 1996; Sethian and Popovici, 1999), a finite-difference solution of the eikonal equation. The inversion scheme is non-linear and repeated iteratively. Prior to the inversion, we deleted data outside the allowed velocity range: 0.5-3.6 km s^{-1} for periods < 10 s; 1.0-4.0 km s^{-1} for periods

200   between 10-20 s; and 2.0-6.0 km s^{-1} for periods 20 s and larger. We derived these thresholds based on the seismic velocity model of an active seismic refraction profile in the centre of the Ligurian Sea (Dannowski et al., 2020). The damping parameter for every period was estimated from L-curves (e.g. Hansen, 1992; Fig. S2). The smoothing parameter was chosen visually depending on the resolution of the inversion (see Table S3 for inversion parameters) and the result of the checkerboard tests. The input error is based on the picking error and linearly increases with the increasing periods from ±0.75-2.0 s. We use

205   homogeneous starting models with period-dependent velocities (Table S2). These are based on a group velocity model calculated from the seismic refraction line by Dannowski et al. (2020). The inversion grid consists of 28x35 nodes, resulting in one node every 18 km for both N-S and W-E directions. Due to grid refinements, the output grids consist of 406x511 grid points. We calculate 2D group velocity maps for 5 s, 6 s, 7 s, 8 s, 9 s, 10 s, 12 s, and 15 s from ambient noise CCFs and 20 s to 90 s in 10 s steps from teleseismic CCFs.

210   In the initial group velocity maps, we observed a low-velocity area west of Marseille associated with station ARBF. We ran a tomography with all ray paths from ARBF excluded, and the result did not show the low-velocity area. Since the station is positioned on sediments in the outer Rhône delta, we assume the low-velocity zone to be caused by a locally 'slower' subsurface. We decided to exclude the station from our dataset to prevent the smearing of local low velocities into the group velocity maps. A similar low-velocity zone was observed close to station A430A, which was excluded as well.

215   In the next step, we use these initial group velocity maps to calculate residuals between the model input and the tomography output. We evaluate the residuals and keep those station pairs corresponding to 1.28 standard deviations (σ; 80 % of all pairs) for periods of 5 s to 15 s. For longer periods, we observe smaller residuals and therefore keep 90 % of the station pairs (1.64 σ). Then, we recalculate the 2D tomographies with the updated dataset to create group velocity maps from ambient noise CCFs. Additionally, we calculated checkerboard tests for every period with tiles of ± 25 % deviation from the input velocity. Synthetic

220   data are calculated and inverted, using the same setup as for the picked data.

1D depth inversion

To remove effects of the highly variable topography and bathymetry, we invert for 1D velocity-depth profiles using the code from Herrmann (2013). We produce dispersion curves for every 10th grid point, resulting in one 1D-v_S-depth-profiles every

225   12.3 km. To account for the non-uniqueness of the solution (Foti et al., 2018), we set up a starting model with fixed layers

Solid Earth
Discussions
Open Access
EGU

(Table S4) that is based on PREM (Dziewonski and Anderson, 1981) at depth and on v_P-velocities from Dannowski et al. (2020) for the shallow layers. Since the dispersion curves for FMST represent a cumulated velocity profile for the subsurface between two stations, it is crucial to correctly parameterise the topography and water column prior to the velocity-depth inversions. To consider the effect of topography and bathymetry, we set up the two uppermost model layers independently:

230 onshore, the top layer reaches from the local elevation to the sea level. The second layer reaches from the sea level to a depth of 4 km. Offshore, the uppermost layer represents the water column with fixed velocities of v_P=1.52 km s^{-1} and v_S=0 km s^{-1}, reaching from the sea surface down to the seafloor, followed by a second layer below reaching from the seafloor down to 4 km depth. Therefore, below 4 km depth, all input models are identical. The layer thicknesses are not varied during the inversion, and the velocity uncertainty is estimated as 2 % of the input group velocity. After parameterisation, we perform iterative 1D

235 depth inversions for v_S (Herrmann, 2013). We obtain 1D velocity-depth profiles from the surface to a depth of 30 km.

3.4 Data Quality

In general, the OBS stations have noise characteristics comparable to land data (Fig. S1). However, we observe that roughly 50 % of all possible CCFs combinations do not show a clear correlation of the group velocities and hence were not considered

240 further. Each OBS is part of combinations resulting in high-quality and low-quality CCFs. Similar effects have been observed by Harmon et al. (2012) and Adimah & Padhy (2020). One reason for this may be the variability in station sites. For the OBS, the water depth is highly variable (1133 m to 2773 m). Also, the characteristics of the seafloor and the coupling to the subsurface are most likely very variable due to the varying sediment thickness beneath each site (Schettino and Turco, 2006). Overall, the essential difference between the LOBSTER OBS stations and most previous studies (e.g. Harmon et al., 2007; Lin

245 et al., 2016) is the shallow location of LOBSTER OBS in the marginal Ligurian Sea. To our knowledge, this study provides the most shallow OBS water depths used for CCFs, and the shallow water might not prove beneficial for the correlation quality. Five stations are at water depths of 2 km or less (the shallowest station A434A is at 1.1 km depth), none is deeper than 2.8 km. Harmon et al. (2012) estimated CCFs of similar quality using OBS stations at 2.5-3.5 km water depth offshore Sumatra. Adimah & Padhy (2020) use OBS in deeper water (14 OBS in 4.3-5.1 km depth and only one OBS at 2.7 km). They observe

250 variations in CCF quality as well, but their overall quality of CCFs is better than for our dataset.

Other reasons for our comparably low CCF quality include the form of the basin itself, for which noise sources are not uniformly distributed, and the highly variable weather conditions of our research area. The Mediterranean Sea lies in a westerly wind system, but especially during winter, mistral events change the flow pattern of regional ocean currents (e.g. Millot & Wald, 1980; André et al., 2005). Moreover, mistral winds might create significant wave heights of 4 m and more (e.g. Pasi et

255 al., 2011). Those temporary changes of the water column and currents alter the pressure on the OBS and the ocean floor and might therefore introduce highly variable noise. Additionally, the land station locations are of varying topography and

geological settings that range from sediment basins to Alpine mountains. Nevertheless, we overall estimated more than 3300 high-quality dispersion curves.

4 Results - Rayleigh wave group velocity maps

We present 3D group velocity and shear-wave velocity information of the Ligurian Sea. We show 2D group velocity maps for periods of 5 s, 8 s, 12 s, 20 s, and 40 s (Fig. 6b-f) accompanied by the tomography input as coloured ray path plots for 8 s (Fig. 6a). The resolvable area is determined from the checkerboard tests (Fig. 7); poorly resolved parts are transparent in the group velocity maps. We use one polygon for all periods. Based on all 2D group velocity maps (5-90 s period), we calculated 1D inversions for shear-wave velocity over depth and created depth slices (Fig. 8).

The ray coverage for ambient noise tomography and the cross-correlation of teleseismic events differs (Fig. 2). Still, the resolved area of both data sets covers the Ligurian Basin and adjacent coastal areas (Fig. 7), whereby the Liguro-Provençal coast is better resolved than the Corsican margin. To increase the resolution at the Liguro-Provençal coast, we added cross-correlations between several land stations. Additionally, this allows us to compare our data with Guerin et al. (2020). At a period of 8 s, Guerin et al. (2020) measured Rayleigh wave group velocities of approximately 3 km s^{-1} for the coastal area, which fits the v_G=2.75-3.2 km s^{-1} found in our study (Fig. 6a) for the same area.

The large-scale structure of our group velocity maps compares well with existing maps. We observe a clear distinction between onshore and offshore areas, especially along the Provençal coast. At a period of 8 s, this is also observed by Molinari et al. (2015b). They found group velocities of less than 2 km s^{-1} in the northeastern Ligurian Basin and $v_G \cong$ 3 km s^{-1} onshore. We observe a similar pattern for periods of 5-12 s (Fig. 6b-d): 1-1.5 km s^{-1} offshore and 2.5-3 km s^{-1} onshore for 5 s and 8 s, 2-2.5 km s-1 offshore and $\geq$ 2.8 km s^{-1} onshore for 12 s. For longer periods (20 s and 40 s, Fig. 6 e,f), the onshore area is approximately 0.5 km s^{-1} slower than the basin. The group velocity maps for periods 20 s and 40 s appear more homogenous than for shorter periods. For 20 s we observe v_G = 3-3.5 km s^{-1}, for 40 s it is v_G = 3.5-4 km s^{-1}. Molinari et al. (2015b) observe similar group velocities for periods of 16-35 s. Since longer periods are sensitive to greater depths (e.g. Adimah & Padhy, 2020), the uniformity might also indicate that the deeper crust and mantle are more homogenous than the upper crust. The onshore-offshore separation is less distinct in the northeastern basin (labelled NE in Fig. 6c), where the group velocity increases gradually towards the coast. Therefore, the marine part appears to be separated into a southwestern (labelled SW in Fig. 6c) and a northeastern part (labelled NE in Fig. 6c) of the Ligurian Basin with an imaginary border roughly from Nice to L'Ile Rousse, Corsica, that prolongs the Alpine front (dashed line in Fig. 6c). We will discuss the different velocity structures of the southwestern and northeastern basin in more detail in Sect. 4.2.

Overall, the group velocity increases with an increasing period. The velocity gradient is strongest (5 s period: $v_G \cong$ 1km s^{-1}; 12 s period: v_G = 2-3 km s^{-1}) beneath the southwestern basin, less strong ($v_G \cong$ 1.75 km s^{-1} to 2.5 km s^{-1}) beneath the northeastern

basin and least strong ($v_G \cong 2.5$ km s^{-1} to 3-3.25 km s^{-1}) beneath the mainland. The variation of the velocity gradient is directly related to the varying crustal thickness.
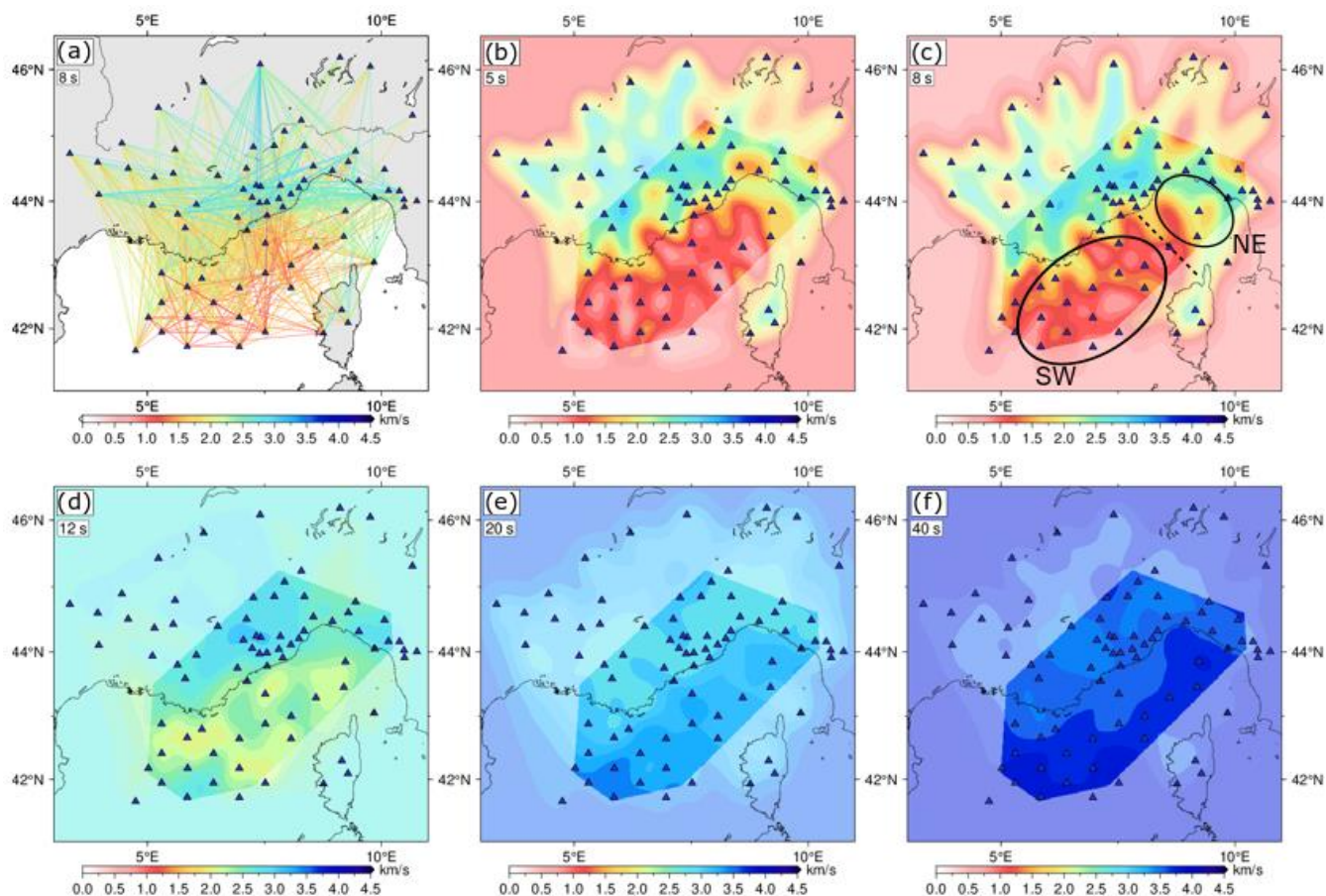
Figure 6: Panel (a) shows the tomography input for 8 s as a ray path plot. Panels (b)-(f) show group velocity maps of the Ligurian Sea from surface wave tomography for 5 s, 8 s, 12 s, 20 s, and 40 s period, whereby (b), (c), and (d) are based on ambient noise cross-correlation and (e) and (f) are based on the cross-correlation of teleseismic events. Areas of low resolution are shown in transparent colours; areas with no ray coverage show the initial velocity (Table S2). Annotations in (c) mark the southwestern and central (SW) and the northeastern (NE) Ligurian Basin. The dashed line represents the proposed prolongation of the Alpine front.
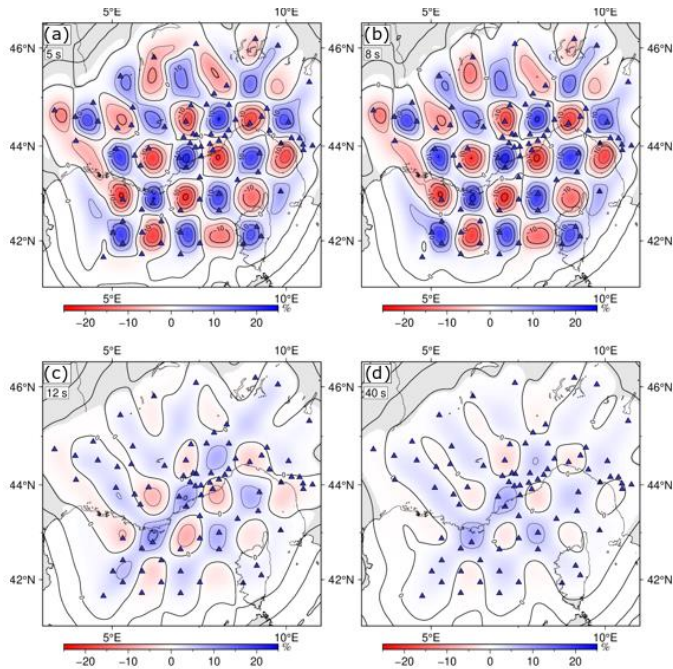
Figure 7: Checkerboard tests for periods of 5 s, 8 s, 12 s, and 40 s (a-d). The perturbation of the input checkerboard tiles is set to ±25 % (the absolute value depends on the period).
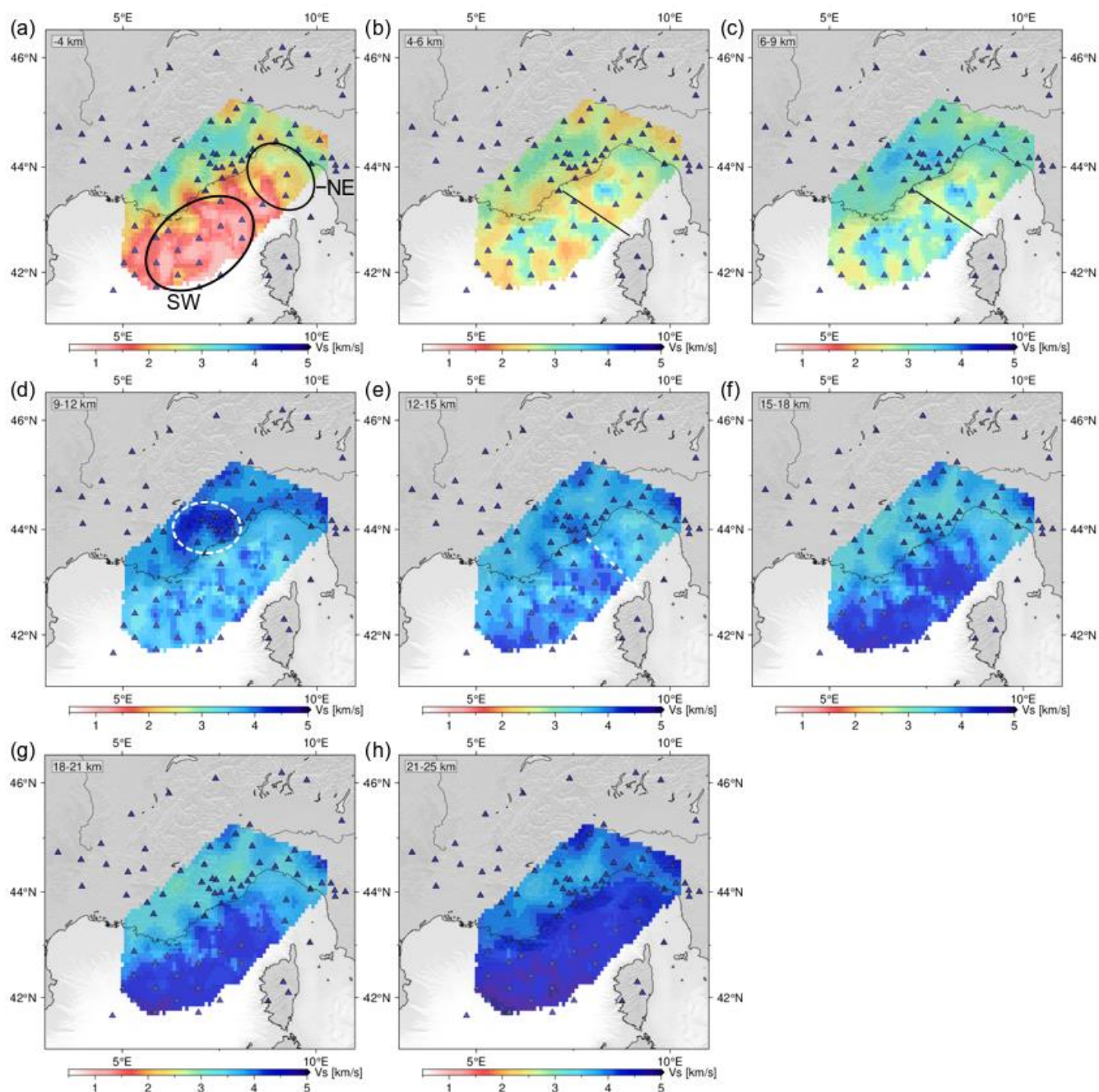
Figure 8: 2D shear velocity maps resulting from the depth inversion. Layer depth is stated in the upper left corner. Depths (in km) are relative to the sea surface. The annotations in (a) mark the southwestern and central (SW) and the northeastern (NE) Ligurian Basin. The solid black line in (b) and (c) show the location of profile LISA01 (Contrucci et al., 2001). The dashed circle in (d) marks a high-velocity area north of Nice (see Sect. 4.2.1), and the dashed line in (e) represents the proposed prolongation of the Alpine front. Layer 1 (topography), layer 10 (25-30 km), and layer 11 (halfspace) are shown in Fig. S3.

305

5 Discussion and Geological interpretation of the shear wave depth layers

310 We calculated 1D depth inversions for v_S based on the group velocity maps described above. In the following, we discuss four distinct regions that show different characteristics in the shear velocity maps. It was a crucial step to remove the topographical effects that result from the amphibious nature of our study area. The average RMS of the 1D inversions is 0.15 km s^{-1}.

5.1 Liguro-Provençal coast

In up to 12-15 km depths, we observe high S-wave velocities beneath the Alpine belt that decrease towards the Rhône delta in
315 the southwest and towards the Po plain in the northeast (Fig. 8a-e). At a depth of 6-9 km below sea level (Fig. 8c), we see v_S $\cong$ 2.75-3 km s^{-1} for the Po plain, $v_S \cong$ 3 km s^{-1} near Marseille, and $v_S \geq$ 3.5 km s^{-1} along the Alpine belt. This S-wave variation is caused by the different geology of the Alpine belt and the sedimentary basins. At the Rhône delta, the sediment cover is up to 12 km thick (Pichon et al., 2010). Similarly, the Po plain has an average sedimentary cover of 7-8 km with a shear-wave velocity of 2.7-3.2 km s^{-1} at 4-10 km depth (Molinari et al., 2015a). In contrast to the sediment basins, we observe higher v_S
320 beneath the Alpine belt, composed of crystalline and metamorphic rocks (e.g. Molinari et al., 2015b). Along the Liguro-Provençal coast, we can compare our results to existing larger-scale ambient noise studies from Molinari et al. (2015b) and Kästle et al. (2018), as well as a local ambient noise study by Guerin et al. (2020). Guerin et al. (2020) conducted an ambient noise study covering the Provençal coast from Marseille to the Argentera Massif north of Nice (Fig. 1). Along the coast, they observe $v_S \cong$ 3-3.5 km s^{-1} at a depth of 6.4 km, comparable to our results. For shallower depths, Guerin et al. (2020) found that
325 the S-wave velocity increases with depth faster than in our data set, a feature that is probably controlled by a denser station spacing compared to our study. Molinari et al. (2015b) present a 3 km depth slice showing $v_S \cong$ 2.7-3 km s^{-1} west of Nice, lower v_S directly at the coast, and an increase in v_S ($v_S \cong$ 3 km s^{-1}) towards the Maures-Esterel Massif (Fig. 1), fitting our results. The 10 km depth slice presented by Molinari et al. (2015b) fits our 6-9 km slice (Fig. 8c). The large-scale structures are also comparable to results of Kästle et al. (2018) and Lu et al. (2018), though in their 10 km depth slice, they observe
330 slightly higher velocities that are closer to those in our 9-12 km depth slice (Fig. 8d). Both our results and Kästle et al. (2018) indicate a narrow band of $v_S \cong$ 3.5 km s^{-1} in 6-9 km depth just onshore Liguria (Fig. 8c), accompanied by lower $v_S \cong$ 3.2 km s^{-1} offshore. Molinari et al. (2015b) observe similar shear-wave velocities offshore, but lower $v_S \cong$ 3 km s^{-1} onshore. Our observation of local high-velocity areas onshore Liguria are supported by seismic refraction profiles evaluated by Laubscher et al. (1992). They identified several high-velocity bodies (v_P > 6 km s^{-1}) linked to ophiolites.
335 We reveal a high-velocity area north of Nice at 9-12 km depth (dashed circle in Fig. 8d), showing $v_S \cong$ 4.2 km s^{-1} coinciding with a small area of higher velocity in the 10 km depth map of Kästle et al. (2018). This is probably linked to the Argentera Massif (Fig. 1). The Massif is composed of crystalline rocks and was identified as a high-velocity area in more shallow depths

($v_S \cong 3.4$ km s^{-1} at 6 km depth) by Guerin et al. (2020). At larger depths, the high-velocity anomaly disappears, and the velocity field along the coastline gets smoother. At 18-21 km depth (Fig. 8g), we observe large areas of v_S = 3.5 km s^{-1}, similar to Molinari et al. (2015b) and Kästle et al. (2018). We observe crustal velocities in 21-25 km depth (Fig. 8h), in line with the Moho depth situated at ~35 km depth beneath the Liguro-Provençal coast (Kästle et al., 2018).

5.2 Southwestern and central Ligurian Basin

In the southwestern and central basin (labelled SW in Fig. 8a), the shear-wave velocities in the uppermost 4 km (Fig. 8a) are ~1.5 km s^{-1}. The velocity increases towards the Provençal coast and the Gulf of Lion. The third layer (4-6 km, Fig. 8b) shows $v_S \cong 2$ km s^{-1} with areas of higher velocity ($v_S \geq 3$ km s^{-1}) offshore Marseille and northwest of Corsica. We assume that sediments mainly dominate the S-wave velocity for the shallow layers. Studies by Schettino & Turco (2006) revealed thick sediment layers in the southwestern Ligurian Basin. Offshore western Corsica, the sediments are 6-7 km thick, with the maximum thickness of 8 km occurring to the southwest of Marseille. This is supported by the findings of Moulin et al. (2015). Their wide-angle reflection seismic data show up to 7.6 km of sediment in the southeastern Gulf of Lion, thinning to 6.3 km in the Ligurian Sea. Throughout the basin, but mainly along the basin axis, we observe areas of higher S-wave velocity of up to 3.5 km s^{-1} in 6-9 km depth (Fig. 8c). Some of these, e.g. north of Corsica, are in locations where Rollet et al. (2002) observe magmatic anomalies related to magmatic intrusions. We deduce that for fast areas along the basin axis, due to the thinning of continental crust, the velocity gradient is stronger than away from the basin axis. This would lead to a higher S-wave velocity near the basin axis.

With increasing depth, the S-wave velocity increases and in 12 km depth, mantle-like $v_S \geq 4.3$ km s^{-1} is reached locally in the basin centre. These fast areas broaden in the 12-15 km depth slice (Fig. 8e), indicating a shallow Moho of ~12 km depth close to the basin axis beneath the southwestern basin. The S-wave velocity is slower towards the Provençal coast, indicating a thicker crust. Dannowski et al. (2020) observe a very similar Moho depth in the basin centre. Comparing their P-wave velocity to our S-wave velocity, we calculate a v_P/v_S-ratio of 7.5/4.3 = 1.74 for the southwestern Ligurian Basin. Following Carlson & Miller (2003), this does not indicate mantle serpentinisation. This is supported by the local seismicity study of Thorwart et al. (2021), that observed v_P=8.1 km s^{-1} and v_S=4.7 km s^{-1} (v_P/v_S=1.72) in the basin centre roughly 3-4 km below the Moho. At 15-18 km depth (Fig. 8f), we observe mantle-like $v_S \geq 4.3$ km s^{-1} along the basin axis of the whole southwestern and central Ligurian Basin. However, v_S is slower (3.7-4 km s^{-1}) south of Marseille and in the outer Gulf of Lion. Also, the "fingers" of high v_S leading from the basin axis towards the coast east and west of Nice are probably caused by an insufficient ray coverage of the group velocity tomography in that area. The ray coverage is better offshore Nice. Therefore, we expect a similar v_S as offshore Nice (v_S = 3.5 km s^{-1}), thus a deeper Moho. At a depth of approximately 21 km (Fig. 8g), $v_S \geq 4.3$ km s^{-1} applies to most of the southwestern and central basin, except for the aforementioned areas. Close to the Provençal coast, the 21-25 km layer (Fig. 8h) indicates a Moho in roughly the mentioned depth.

Contrucci et al. (2001) investigated a multichannel seismic profile (LISA01) from Antibes, close to Nice, to L'Île Rousse on Corsica (Fig. 1 and Fig. 8b-c), crossing the central Ligurian Basin. They find that the transition from sediments to crust (at v_P

16

~ 4.8-5 km s^{-1}) is shallow at the Provençal coast (3 km below sea level), deepens towards the basin centre (8 km below sea level), and rapidly shallows again at the Corsican margin (from 5 km to 1.5 km below sea level). Also, the salt (Messinian) and sediment (Miocene) layers (v$_P$ = 3.8 km s^{-1} to 5 km s^{-1}) thicken towards the basin centre (Contrucci et al., 2001), where the Moho is ~12-13 km deep. Our v$_S$ maps for 4-9 km depth (Fig. 8b-c) show a local velocity high with increasing v$_S$ (2.75-3 km s^{-1}) directly offshore Nice. Further southeast along the LISA01 profile (Fig. 8b-c, solid black line), the velocity decreases to v$_S$ ≅ 2.1 km s^{-1} in 4-6 km depth and v$_S$ ≅ 2.5-2.7 km s^{-1} in 6-9 km depth. The resolution is sparse at the Corsican margin, but v$_S$ increases to 3 km s^{-1} towards Corsica (Fig. 8c). We estimate the Moho to be ~ 12-15 km deep (Fig. 8e). The observed velocity structure fits the findings of Contrucci et al. (2001) nicely, supporting their finding of thicker sediment and salt layers near the basin axis. Comparing v$_P$ of the LISA01 profile to our v$_S$ gives a v$_P$/v$_S$-ratio of 1.75 for the high-velocity area offshore Nice and v$_P$/v$_S$ ≅ 2.1 for the sediment layers at the basin axis. Shillington et al. (2007) found similar values for sediments up to 1 km below seafloor.

5.3 Northeastern basin

Northeast of the LISA01 profile, the northeastern basin (labelled NE in Fig. 8a) exhibits different characteristics than the southwestern and central Ligurian Basin. The shear-wave velocity is higher than in the southwest for shallow depths. North of Corsica, v$_S$ ≅ 2 km s^{-1} in up to 4 km depth (Fig. 8a) with higher velocity v$_S$ ≅ 2.5 km s^{-1} close to the coast. The velocity increases to v$_S$ ≅ 3 km s^{-1} at 4-6 km depth (Fig. 8b) and v$_S$ = 3.3 km s^{-1} at 6-9 km below the sea surface (Fig. 8c). At 9-21 km depth (Fig. 8d-g), v$_S$ appears to increase slowly from 3.5 km s^{-1} to 3.8 km s^{-1}. From approximately 12-15 km on (Fig. 8e), v$_S$ is lower close to the coast than towards the south-eastern basin. At 21-25 km depth (Fig. 8h), v$_S$ ≥ 4.3 km s^{-1} is similar to the southwestern basin except for a narrow band at the Ligurian coast that shows lower velocities of v$_S$ ≅ 4 km s^{-1}. Our results are supported by large-scale ambient noise studies by Molinari et al. (2015b) and Kästle et al. (2018). Overall, the northeastern basin is more homogenous than the southwest, and the transition from the basin to onshore Italy is not as sharp as for the Provençal coastline. The higher v$_S$ at shallow depths, compared to the southwest, implies that the sediment cover is thinner in the northeastern basin. This is supported by the sediment thickness map by Schettino & Turco (2006), showing a sediment thickness of 3-4 km in the northeast, increasing to the southwest. Therefore, we observe crustal velocities beginning at 4-6 km depth for most of the northeastern basin and even shallower locally.

We observe mantle-like v$_S$ ≥ 4.3 km s^{-1} in the central southwestern basin starting at about 12 km depth (Fig. 8d-e). Towards the northeast, the depth when S-wave velocities of v$_S$ ≥ 4.3 km s^{-1} are reached increases (Fig. 8e-h). We interpret this as a north-eastward thickening of the continental crust beneath the Ligurian Sea. We conclude a Moho depth of 12 km along the basin axis beneath the southwestern Ligurian Basin. The Moho depth increases from the basin axis towards the Provençal coast (~12 km to at least 25 km at the coast) and the northeast. Close to the Ligurian coast, the Moho reaches a depth of about 21-25 km. At the coastline, the crust is even thicker, as Kästle et al. (2018) predict. The observation of a north-eastwards thickening continental crust is in line with results from gravity modelling by Dannowski et al. (2020) along their refraction seismic line

(Fig. 1) and the prolonging wide-angle reflection seismic line by Makris et al. (1999). Both experiments reveal similar values

405 for the Moho depth, explaining satellite-derived free-air anomaly (Sandwell et al., 2014) by a gradual thickening of continental

crust towards the northeast, reaching a Moho depth of 22 km close to the Italian coast.

The apparent thickening of the continental crust towards the northeast is likely related to the position of the rotational pole of

the opening of the Ligurian Sea during Oligocene-Miocene times. According to Garracceca et al. (2007), the rotational pole

was located in the northeastern Ligurian Sea at 43.5°N, 9.5°E. Therefore, the southwestern basin was more extensively opened,

410 and the continental crust was thinned further than in the northeast.

5.4 Alpine front

Rollet et al. (2002) raised the question of an offshore prolongation of the Alpine front that can be observed onshore France

and onshore Corsica. Rollet et al. (2002) suggested the Alpine front to separate the southwestern and northeastern parts of the

415 Ligurian Basin. However, the location and even existence of such a prolongation of the Alpine front beneath the Ligurian sea

is not yet resolved. If it existed, it should be located beneath the crust and be visible as a velocity anomaly in the upper mantle.

The location of the Alpine front offshore should prolong the onshore front (Fig. 1) and hence be perpendicular to the basin

axis. Therefore, it should be visible in the velocity model as an NW-SE trending positive anomaly (Kästle et al., 2018) and

perpendicular to the features related to the opening of the Ligurian Sea. According to Kästle et al. (2018, Fig. 9), in 10 km

420 depth, the S-wave velocity contrast onshore is 0.5 km s^{-1} and the anomaly is ~50 km wide. We observe a similar velocity

contrast beneath the Alpine belt, but do not see this contrast continued offshore. Therefore, we do not find evidence for an

Alpine slab beneath the Ligurian Sea (Fig. 8). However, the group- and shear-velocity maps suggest a separation of the

northeastern and southwestern crustal domain along an imaginable line roughly from Nice to the northern tip of Corsica

(dashed lines in Fig. 6c and Fig. 8e), prolonging the onshore Alpine front (Fig. 1).

425

6 Conclusions

Applying ambient noise techniques and the correlation of teleseismic events to amphibious data results in the first 3D high-

resolution seismic group and shear velocity models for the Ligurian Sea. Data processing of the OBS data included correction

for tilt and compliance. The dataset differs from most previous ambient noise studies using OBS data that we find, insofar as

430 our stations are comparably shallow and the fundamental mode is not always the most prominent signal in the marine ray

paths. Higher modes are primarily observed in the southeast. Onshore, our results compare well with existing larger-scale

ambient noise studies. We reveal a high-velocity area at the Argentera Massif, approximately 10 km below sea level. Offshore,

the lithospheric structure in the Ligurian Basin mostly mimics the geometry of the basin. Shear-wave velocity maps indicate a

gradual deepening of the Moho from 12-15 km in the southwestern basin centre towards 20-25 km in the northeastern basin

435 and a more rapid deepening from the basin axis to the Provençal coast (> 30 km). Based on the low v_P/v_S ratios of 1.74, we exclude mantle serpentinisation in the basin centre. Overall, the off-shore region north of Corsica is faster than the southwestern basin at shallow depths (<12 km) and slower below. To the southwestern part, the opening of the basin is more developed. The change between these domains appears gradual and is located above the assumed prolongation of the Alpine front. Down to depths of 25 km, we do not see evidence for an Alpine slab in the Ligurian Sea.

Data availability

The data can be accessed via GEOFON and EIDA Data Archives. Data from AlpArray stations (including the OBSs) are accessible to AlpArray members. They will be freely accessible after March 2022.

Team list

445 Full list of the AlpArray Working Group: György HETÉNYI, Rafael ABREU, Ivo ALLEGRETTI, Maria-Theresia APOLONER, Coralie AUBERT, Simon BESANÇON, Maxime BÈS DE BERC, Götz BOKELMANN, Didier BRUNEL, Marco CAPELLO, Martina ČARMAN, Adriano CAVALIERE, Jérôme CHÈZE, Claudio CHIARABBA, John CLINTON, Glenn COUGOULAT, Wayne C. CRAWFORD, Luigia CRISTIANO, Tibor CZIFRA, Ezio D'ALEMA, Stefania DANESI, Romuald DANIEL, Anke DANNOWSKI, Iva DASOVIĆ, Anne DESCHAMPS, Jean-Xavier DESSA, Cécile DOUBRE, Sven EGDORF, ETHZ-SED Electronics Lab, Tomislav FIKET, Kasper FISCHER, Wolfgang FRIEDERICH, Florian FUCHS, Sigward FUNKE, Domenico GIARDINI, Aladino GOVONI, Zoltán GRÁCZER, Gidera GRÖSCHL, Stefan HEIMERS, Ben HEIT, Davorka HERAK, Marijan HERAK, Johann HUBER, Dejan JARIĆ, Petr JEDLIČKA, Yan JIA, Hélène JUND, Edi KISSLING, Stefan KLINGEN, Bernhard KLOTZ, Petr KOLÍNSKÝ, Heidrun KOPP, Michael KORN, Josef KOTEK, Lothar KÜHNE, Krešo KUK, Dietrich LANGE, Jürgen LOOS, Sara LOVATI, Deny MALENGROS, Lucia MARGHERITI, Christophe MARON, Xavier MARTIN, Marco MASSA, Francesco MAZZARINI, Thomas MEIER, Laurent MÉTRAL, Irene MOLINARI, Milena MORETTI, Anna NARDI, Jurij PAHOR, Anne PAUL, Catherine PÉQUEGNAT, Daniel PETERSEN, Damiano PESARESI, Davide PICCININI, Claudia PIROMALLO, Thomas PLENEFISCH, Jaroslava PLOMEROVÁ, Silvia PONDRELLI, Snježan PREVOLNIK, Roman RACINE, Marc RÉGNIER, Miriam REISS, Joachim RITTER, Georg RÜMPKER, Simone SALIMBENI, Marco SANTULIN, Werner SCHERER, Sven SCHIPPKUS, Detlef SCHULTE-KORTNACK, Vesna ŠIPKA, Stefano SOLARINO, Daniele SPALLAROSSA, Kathrin SPIEKER, Josip STIPČEVIĆ, Angelo STROLLO, Bálint SÜLE, Gyöngyvér SZANYI, Eszter SZŰCS, Christine THOMAS, Martin THORWART, Frederik TILMANN, Stefan UEDING, Massimiliano VALLOCCHIA, Luděk VECSEY, René VOIGT, Joachim WASSERMANN, Zoltán WÉBER, Christian

Solid Earth
Discussions

Open Access

EGU

WEIDLE, Viktor WESZTERGOM, Gauthier WEYLAND, Stefan WIEMER, Felix Noah WOLF, David WOLYNIEC,
465 Thomas ZIEKE, Mladen ŽIVČIĆ, Helena ŽLEBČÍKOVÁ

Author contribution

DL, MT, IG and HK were responsible for the conception of this study. DL, WC, AD, and HK were responsible for the design of the OBS network. FNW, DL, AD, MT, WC, and HK participated in acquiring OBS data. FNW analysed the data with the support of all co-authors. WC and LW provided software and expertise for the compliance correction and MFT. All authors
470 interpreted the data. FNW prepared the manuscript, and all authors critically reviewed it.

Competing interests

The authors declare that they have no conflict of interest.

Acknowledgements

20

Solid Earth
Discussions

Open Access

EGU

References

490

Adimah, N. I. and Padhy, S.: Ambient noise Rayleigh wave tomography across the Madagascar island, Geophys. J. Int., 220, 1657–1676, https://doi.org/10.1093/gji/ggz542, 2020.

Aki, K.: Space and Time Spectra of Stationary Stochastic Waves, with Special Reference to Microtremors, Bull Earthq. Res Inst Univ Tokyo, 415–456, 1957.

495 André, G., Garreau, P., Garnier, V., and Fraunié, P.: Modelled variability of the sea surface circulation in the North-western Mediterranean Sea and in the Gulf of Lions, Ocean Dyn., 55, 294–308, https://doi.org/10.1007/s10236-005-0013-6, 2005.

Barmin, M. P., Ritzwoller, M. H., and Levshin, A. L.: A Fast and Reliable Method for Surface Wave Tomography, in: Monitoring the Comprehensive Nuclear-Test-Ban Treaty: Surface Waves, Birkhäuser Basel, Basel, 1351–1375, https://doi.org/10.1007/978-3-0348-8264-4_3, 2001.

500 Bell, S. W., Forsyth, D. W., and Ruan, Y.: Removing Noise from the Vertical Component Records of Ocean-Bottom Seismometers: Results from Year One of the Cascadia Initiative, Bull. Seismol. Soc. Am., 105, 300–313, https://doi.org/10.1785/0120140054, 2015.

Bensen, G. D., Ritzwoller, M. H., Barmin, M. P., Levshin, A. L., Lin, F., Moschetti, M. P., Shapiro, N. M., and Yang, Y.: Processing seismic ambient noise data to obtain reliable broad-band surface wave dispersion measurements, Geophys. J. Int.,
505 169, 1239–1260, https://doi.org/10.1111/j.1365-246X.2007.03374.x, 2007.

Beyreuther, M., Barsch, R., Krischer, L., Megies, T., Behr, Y., and Wassermann, J.: ObsPy: A Python Toolbox for Seismology, Seismol. Res. Lett., 81, 530–533, https://doi.org/10.1785/gssrl.81.3.530, 2010.

Campillo, M. and Paul, A.: Long-Range Correlations in the Diffuse Seismic Coda, Science, 299, 547–549, https://doi.org/10.1126/science.1078551, 2003.

510 Campillo, M. and Roux, P.: Seismic Imaging and Monitoring with Ambient Noise Correlations, in: Treatise on Geophysics, 2016.

Carlson, R. L. and Miller, D. J.: Mantle wedge water contents estimated from seismic velocities in partially serpentinized peridotites, Geophys. Res. Lett., 30, 12–15, https://doi.org/10.1029/2002gl016600, 2003.

Contrucci, I., Nercessian, A., Béthoux, N., Mauffret, A., and Pascal, G.: A Ligurian (Western Mediterranean Sea) geophysical
515 transect revisited, Geophys. J. Int., 146, 74–97, https://doi.org/10.1046/j.0956-540x.2001.01418.x, 2001.

Cox, C., Deaton, T., and Webb, S.: A Deep-Sea Differential Pressure Gauge, J. Atmospheric Ocean. Technol., 1, 237–246, https://doi.org/10.1175/1520-0426(1984)001<0237:ADSDPG>2.0.CO;2, 1984.

Crawford, W. C. and Webb, S. C.: Identifying and Removing Tilt Noise from Low-Frequency (<0.1 Hz) Seafloor Vertical Seismic Data, Bull. Seismol. Soc. Am., 90, 952–963, https://doi.org/10.1785/0119990121, 2000.

520 Crawford, W. C., Webb, S. C., and Hildebrand, J. A.: Estimating shear velocities in the oceanic crust from compliance measurements by two-dimensional finite difference modeling, J. Geophys. Res. Solid Earth, 103, 9895–9916, https://doi.org/10.1029/97JB03532, 1998.

Dannowski, A., Kopp, H., Grevemeyer, I., Lange, D., Thorwart, M., Bialas, J., and Wollatz-Vogt, M.: Seismic evidence for failed rifting in the Ligurian Basin, Western Alpine domain, Solid Earth, 11, 873–887, https://doi.org/10.5194/se-11-873-2020, 2020.

Dewangan, P., Reddy, R., Kamesh Raju, K. A., Singha, P., Aswini, K. K., Yatheesh, V., Samudrala, K., and Shuhail, M.: Nature of the Ambient Noise, Site Response, and Orientation of Ocean-Bottom Seismometers (OBSs): Scientific Results of a Passive Seismic Experiment in the Andaman Sea, Bull. Seismol. Soc. Am., 108, 248–259, https://doi.org/10.1785/0120170163, 2018.

Dziewonski, A. M. and Anderson, D. L.: Preliminary reference Earth model, Phys. Earth Planet. Inter., 25, 297–356, https://doi.org/10.1016/0031-9201(81)90046-7, 1981.

Dziewonski, A. M., Bloch, S., and Landisman, M.: A Technique for the Analysis of Transient Seismic Signals, Bull. Seismol. Soc. Am., 59, 427–444, 1969.

Faccenna, C., Funiciello, F., Giardini, D., and Lucente, P.: Episodic back-arc extension during restricted mantle convection in the Central Mediterranean, Earth Planet. Sci. Lett., 187, 105–116, https://doi.org/10.1016/S0012-821X(01)00280-1, 2001.

Foti, S., Hollender, F., Garofalo, F., Albarello, D., Asten, M., Bard, P. Y., Comina, C., Cornou, C., Cox, B., Di Giulio, G., Forbriger, T., Hayashi, K., Lunedei, E., Martin, A., Mercerat, D., Ohrnberger, M., Poggi, V., Renalier, F., Sicilia, D., and Socco, V.: Guidelines for the good practice of surface wave analysis: a product of the InterPACIFIC project, Bull. Earthq. Eng., 16.6, 2367–2420, https://doi.org/10.1007/s10518-017-0206-7, 2018.

Gailler, A., Klingelhoefer, F., Olivet, J.-L. L., and Aslanian, D.: Crustal structure of a young margin pair: New results across the Liguro–Provencal Basin from wide-angle seismic tomography, Earth Planet. Sci. Lett., 286, 333–345, https://doi.org/10.1016/j.epsl.2009.07.001, 2009.

Gattacceca, J., Deino, A., Rizzo, R., Jones, D. S., Henry, B., Beaudoin, B., and Vadeboin, F.: Miocene rotation of Sardinia: New paleomagnetic and geochronological constraints and geodynamic implications, Earth Planet. Sci. Lett., 258, 359–377, https://doi.org/10.1016/j.epsl.2007.02.003, 2007.

Goutorbe, B., de Oliveira Coelho, D. L., and Drouet, S.: Rayleigh wave group velocities at periods of 6–23 s across Brazil from ambient noise tomography, Geophys. J. Int., 203, 869–882, https://doi.org/10.1093/gji/ggv343, 2015.

Gueguen, E., Doglioni, C., and Fernandez, M.: On the post-25 Ma geodynamic evolution of the western Mediterranean, Tectonophysics, 298, 259–269, https://doi.org/10.1016/S0040-1951(98)00189-9, 1998.

Guerin, G., Rivet, D., Deschamps, A., Larroque, C., Mordret, A., Dessa, J.-X., and Martin, X.: High resolution ambient noise tomography of the Southwestern Alps and the Ligurian margin, Geophys. J. Int., 220, 806–820, https://doi.org/10.1093/gji/ggz477, 2020.

Hansen, P. C.: Analysis of Discrete Ill-Posed Problems by Means of the L-Curve, SIAM Rev., 34, 561–580, https://doi.org/10.1137/1034115, 1992.

555   Harmon, N., Forsyth, D., and Webb, S.: Using Ambient Seismic Noise to Determine Short-Period Phase Velocities and Shallow Shear Velocities in Young Oceanic Lithosphere, Bull. Seismol. Soc. Am., 97, 2009–2023, https://doi.org/10.1785/0120070050, 2007.

Harmon, N., Henstock, T., Tilmann, F., Rietbrock, A., and Barton, P.: Shear velocity structure across the Sumatran Forearc-Arc, Geophys. J. Int., 189, 1306–1314, https://doi.org/10.1111/j.1365-246X.2012.05446.x, 2012.

560   Herrmann, R. B.: Computer Programs in Seismology: An Evolving Tool for Instruction and Research, Seismol. Res. Lett., 84, 1081–1088, https://doi.org/10.1785/0220110096, 2013.

Hetényi, G., Molinari, I., Clinton, J., Bokelmann, G., Bondár, I., Crawford, W. C., Dessa, J.-X., Doubre, C., Friederich, W., Fuchs, F., Giardini, D., Gráczer, Z., Handy, M. R., Herak, M., Jia, Y., Kissling, E. E., Kopp, H., Korn, M., Margheriti, L., Meier, T., Mucciarelli, M., Paul, A., Pesaresi, D., Piromallo, C., Plenefisch, T., Plomerová, J., Ritter, J., Rümpker, G., Šipka, V., Spallarossa, D., Thomas, C., Tilmann, F., Wassermann, J., Weber, M., Wéber, Z., Wesztergom, V., and Živčić, M.: The AlpArray Seismic Network: A Large-Scale European Experiment to Image the Alpine Orogen, Surv. Geophys., 39, 1009–1033, https://doi.org/10.1007/s10712-018-9472-4, 2018.

Jolivet, L. and Faccenna, C.: Mediterranean extension and the Africa-Eurasia collision, Tectonics, 19, 1095–1106, https://doi.org/10.1029/2000TC900018, 2000.

570   Jolivet, L., Gorini, C., Smit, J., and Leroy, S.: Continental breakup and the dynamics of rifting in back-arc basins: The Gulf of Lion margin, Tectonics, 34, 662–679, https://doi.org/10.1002/2014TC003570, 2015.

Kästle, E. D., El-Sharkawy, A., Boschi, L., Meier, T., Rosenberg, C., Bellahsen, N., Cristiano, L., and Weidle, C.: Surface Wave Tomography of the Alps Using Ambient-Noise and Earthquake Phase Velocity Measurements, J. Geophys. Res. Solid Earth, 123, 1770–1792, https://doi.org/10.1002/2017JB014698, 2018.

575   Kästle, E. D., Rosenberg, C., Boschi, L., Bellahsen, N., Meier, T., and El-Sharkawy, A.: Slab Break-offs in the Alpine Subduction Zone, Solid Earth Discuss., 1–16, https://doi.org/10.5194/se-2019-17, 2019.

Krischer, L., Megies, T., Barsch, R., Beyreuther, M., Lecocq, T., Caudron, C., and Wassermann, J.: ObsPy: a bridge for seismology into the scientific Python ecosystem, Comput. Sci. Discov., 8, 014003–014003, https://doi.org/10.1088/1749-4699/8/1/014003, 2015.

580   Laubscher, H., Biella, G. C., Cassinis, R., Gelati, R., Lozej, A., Scarascia, S., and Tabacco, I.: The collisional knot in Liguria, Geol. Rundsch., 81, 275–289, https://doi.org/10.1007/BF01828598, 1992.

Lin, P.-Y. P., Gaherty, J. B., Jin, G., Collins, J. A., Lizarralde, D., Evans, R. L., and Hirth, G.: High-resolution seismic constraints on flow dynamics in the oceanic asthenosphere, Nature, 535, 538–541, https://doi.org/10.1038/nature18012, 2016.

Lobkis, O. I. and Weaver, R. L.: On the emergence of the Green's function in the correlations of a diffuse field, J. Acoust. Soc.
585   Am., 110, 3011–3017, https://doi.org/10.1121/1.1417528, 2001.

Lu, Y., Stehly, L., and Paul, A.: High-resolution surface wave tomography of the European crust and uppermost mantle from ambient seismic noise, Geophys. J. Int., 214, 1136–1150, https://doi.org/10.1093/gji/ggy188, 2018.

Makris, J., Egloff, F., Nicolich, R., and Rihm, R.: Crustal structure from the Ligurian Sea to the Northern Apennines — a wide angle seismic transect, Tectonophysics, 301, 305–319, https://doi.org/10.1016/S0040-1951(98)00225-X, 1999.

590   McNamara, D. E. and Buland, R. P.: Ambient Noise Levels in the Continental United States, Bull. Seismol. Soc. Am., 94, 1517–1527, https://doi.org/10.1785/012003001, 2004.

Meier, T., Dietrich, K., Stöckhert, B., and Harjes, H. P.: One-dimensional models of shear wave velocity for the eastern Mediterranean obtained from the inversion of Rayleigh wave phase velocities and tectonic implications, Geophys. J. Int., 156, 45–58, https://doi.org/10.1111/j.1365-246X.2004.02121.x, 2004.

595   Millot, C. and Wald, L.: The effects of Mistral wind on the Ligurian current near Provence, Oceanol. Acta, 3, 399–402, 1980.

Molinari, I., Argnani, A., Morelli, A., and Basini, P.: Development and Testing of a 3D Seismic Velocity Model of the Po Plain Sedimentary Basin, Italy, Bull. Seismol. Soc. Am., 105, 753–764, https://doi.org/10.1785/0120140204, 2015a.

Molinari, I., Verbeke, J., Boschi, L., Kissling, E., and Morelli, A.: Italian and Alpine three-dimensional crustal structure imaged by ambient-noise surface-wave dispersion, Geochem. Geophys. Geosystems, 16, 4405–4421,
600   https://doi.org/10.1002/2015GC006176, 2015b.

Moulin, M., Klingelhoefer, F., Afilhado, A., Aslanian, D., Schnurle, P., Nouzé, H., Rabineau, M., Beslier, M.-O., and Feld, A.: Deep crustal structure across a young passive margin from wide-angle and reflection seismic data (The SARDINIA Experiment) – I. Gulf of Lion's margin, Bull. Société Géologique Fr., 186, 309–330, https://doi.org/10.2113/gssgfbull.186.4-5.309, 2015.

605   Pasi, F., Orlandi, A., Onorato, L. F., and Gallino, S.: A study of the 1 and 2 January 2010 sea-storm in the Ligurian Sea, Adv. Sci. Res., 109–115, https://doi.org/10.5194/asr-6-109-2011, 2011.

Pichon, X. L., Rangin, C., Hamon, Y., Loget, N., Lin, J. Y., Andreani, L., and Flotte, N.: Geodynamics of the France Southeast Basin, Bull Soc Géol Fr, 25, 2010.

Prieto, G. A., Lawrence, J. F., and Beroza, G. C.: Anelastic Earth structure from the coherency of the ambient seismic field, J.
610   Geophys. Res., 114, B07303–B07303, https://doi.org/10.1029/2008JB006067, 2009.

Rawlinson, N. and Sambridge, M.: Wave front evolution in strongly heterogeneous layered media using the fast marching method, Geophys. J. Int., 156, 631–647, https://doi.org/10.1111/j.1365-246X.2004.02153.x, 2004.

Rawlinson, N. and Sambridge, M.: The fast marching method: an effective tool for tomographic imaging and tracking multiple phases in complex layered media, Explor. Geophys., 36, 341–350, https://doi.org/10.1071/EG05341, 2005.

615   Rollet, N., Déverchère, J., Beslier, M.-O., Guennoc, P., Réhault, J.-P., Sosson, M., and Truffert, C.: Back arc extension, tectonic inheritance, and volcanism in the Ligurian Sea, Western Mediterranean, Tectonics, 21, 6-1-6–23, https://doi.org/10.1029/2001TC900027, 2002.

Rosenbaum, G., Lister, G. S., and Duboz, C.: Reconstruction of the tectonic evolution of the western Mediterranean since the Oligocene, J. Virtual Explor., 08, 107–126, https://doi.org/10.3809/jvirtex.2002.00053, 2002.

620   Ryan, W. B. F., Carbotte, S. M., Coplan, J. O., O'Hara, S., Melkonian, A., Arko, R., Weissel, R. A., Ferrini, V., Goodwillie, A., Nitsche, F., Bonczkowski, J., and Zemsky, R.: Global Multi-Resolution Topography synthesis, Geochem. Geophys. Geosystems, 10, n/a-n/a, https://doi.org/10.1029/2008GC002332, 2009.

Sandwell, D. T., Müller, R. D., Smith, W. H. F., Garcia, E., and Francis, R.: New global marine gravity model from CryoSat-2 and Jason-1 reveals buried tectonic structure, Science, 346, 65–67, https://doi.org/10.1126/science.1258213, 2014.

625   Schettino, A. and Turco, E.: Plate kinematics of the Western Mediterranean region during the Oligocene and Early Miocene, Geophys. J. Int., 166, 1398–1423, https://doi.org/10.1111/j.1365-246X.2006.02997.x, 2006.

Schmid, S. M., Fügenschuh, B., Kissling, E., and Schuster, R.: Tectonic map and overall architecture of the Alpine orogen, Eclogae Geol. Helvetiae, 97, 93–117, https://doi.org/10.1007/s00015-004-1113-x, 2004.

Sethian, J. A.: A fast marching level set method for monotonically advancing fronts., Proc. Natl. Acad. Sci., 93, 1591–1595,
630   https://doi.org/10.1073/pnas.93.4.1591, 1996.

Sethian, J. A. and Popovici, A. M.: 3-D traveltime computation using the fast marching method, GEOPHYSICS, 64, 516–523, https://doi.org/10.1190/1.1444558, 1999.

Shapiro, N. M., Campillo, M., Stehly, L., and Ritzwoller, M. H.: High-Resolution Surface-Wave Tomography from Ambient Seismic Noise, Science, 307, 1615–1618, https://doi.org/10.1126/science.1108339, 2005.

635   Shillington, D. J., Minshull, T. A., Peirce, C., and O'Sullivan, J. M.: P- and S-wave velocities of consolidated sediments from a seafloor seismic survey in the North Celtic Sea Basin, offshore Ireland, Geophys. Prospect., 56, 197–211, https://doi.org/10.1111/j.1365-2478.2007.00669.x, 2007.

Stähler, S. C., Sigloch, K., Hosseini, K., Crawford, W. C., Barruol, G., Schmidt-Aursch, M. C., Tsekhmistrenko, M., Scholz, J.-R. R., Mazzullo, A., and Deen, M.: Performance report of the RHUM-RUM ocean bottom seismometer network around La
640   Réunion, western Indian Ocean, Adv. Geosci., 41, 43–63, https://doi.org/10.5194/adgeo-41-43-2016, 2016.

Takeo, A., Forsyth, D. W., Weeraratne, D. S., and Nishida, K.: Estimation of azimuthal anisotropy in the NW Pacific from seismic ambient noise in seafloor records, Geophys. J. Int., 199, 11–22, https://doi.org/10.1093/gji/ggu240, 2014.

Thorwart, M., Dannowski, A., Grevemeyer, I., Lange, D., Kopp, H., Petersen, F., Crawford, W., Paul, A., and the AlpArray Working Group: Basin inversion: Reactivated rift structures in the Ligurian Searevealed by OBS, Solid Earth Discuss.,
645   https://doi.org/10.5194/se-2021-9, 2021.

Tonegawa, T., Yamashita, Y., Takahashi, T., Shinohara, M., Ishihara, Y., Kodaira, S., and Kaneda, Y.: Spatial relationship between shallow very low frequency earthquakes and the subducted Kyushu-Palau Ridge in the Hyuga-nada region of the Nankai subduction zone, Geophys. J. Int., 222, 1542–1554, https://doi.org/10.1093/gji/ggaa264, 2020.

Vigliotti, L. and Langenheim, V. E.: When did Sardinia stop rotating? New palaeomagnetic results, Terra Nova, 7, 424–435,
650   https://doi.org/10.1111/j.1365-3121.1995.tb00538.x, 1995.

Wapenaar, K., Draganov, D., Snieder, R., Campman, X., and Verdel, A.: Tutorial on seismic interferometry: Part 1 — Basic principles and applications, GEOPHYSICS, 75, 75A195-75A209, https://doi.org/10.1190/1.3457445, 2010a.

Wapenaar, K., Slob, E., Snieder, R., and Curtis, A.: Tutorial on seismic interferometry: Part 2 — Underlying theory and new advances, GEOPHYSICS, 75, 75A211-75A227, https://doi.org/10.1190/1.3463440, 2010b.

655   Webb, S. C.: Broadband seismology and noise under the ocean, Rev. Geophys., 36, 105–142, https://doi.org/10.1029/97RG02287, 1998.

Webb, S. C. and Crawford, W. C.: Long-period seafloor seismology and deformation under ocean waves, Bull. Seismol. Soc. Am., 89, 1535–1542, 1999.